Chinese Chemical Letters 31 (2020) 2705–2711

Contents lists available at ScienceDirect

Chinese Chemical Letters

journal homepage: www.elsevier.com/locate/cclet

Communication

Novel synthesis of Z-scheme α-Bi_2O_3/g-C_3N_4 composite photocatalyst and its enhanced visible light photocatalytic performance: Influence of calcination temperature

Bo Li[a], Li-Chao Nengzi[b], Ruonan Guo[a], Yuqi Cui[a], Youxian Zhang[a,*], Xiuwen Cheng[a,b,*]

[a] Key Laboratory of Western China's Environmental Systems (Ministry of Education) and Key Laboratory for Environmental Pollution Prediction and Control, Gansu Province, College of Earth and Environmental Sciences, Lanzhou University, Lanzhou 730000, China
[b] Academy of Economics and Environmental Sciences, Xichang University, Xichang 615000, China

ARTICLE INFO

Article history:
Received 8 March 2020
Received in revised form 31 March 2020
Accepted 13 April 2020
Available online 23 April 2020

Keywords:
α-Bi_2O_3/g-C_3N_4
Photocatalysis
Calcination temperature
Z-scheme

ABSTRACT

In this study, α-Bi_2O_3/g-C_3N_4 nanocomposite with direct Z-scheme was successfully prepared through calcination of BiOCOOH/g-C_3N_4 precursor at different temperature. Meanwhile, the effect of calcination temperature on the physicochemical properties of α-Bi_2O_3/g-C_3N_4 was studied. All results confirmed that calcination temperature greatly influences structural, morphology, surface states, photoelectrochemical property and photocatalytic (PC) performance of α-Bi_2O_3/g-C_3N_4 composite. Furthermore, the α-Bi_2O_3/g-C_3N_4 composite was applied as photocatalyst to degrade amido black 10B dye under visible light irradiation. It was found that the composite synthesized at 400 °C exhibited the highest PC performance due to the intense visible light absorbance and high separation efficiency of electron and hole pairs. Besides, the possible PC mechanism was proposed that the photo-generated charge carrier migration in α-Bi_2O_3/g-C_3N_4 photocatalyst followed a Z-scheme structure. Finally, the stability test also manifest that the α-Bi_2O_3/g-C_3N_4 composite photocatalyst has good stability and reusability, which was a promising candidate for wastewater treatment.

At present, the rapid consumption of natural resources and the intensification of environmental pollution have seriously affected the society development as well as ecosystem and human health [1]. However, conventional physicochemical technologies are not so effective in removal of these environmental concerns [2,3]. Therefore, exploring advanced strategies to ease this dilemma is imperative. As typical environmentally friendly technology, several kinds of advanced oxidation processes (AOP) technologies have been extensively used in various fields for pollutant removal. In particular, semiconductor-based photocatalysis was recognized as the most promising one because of its high efficiency, economic feasibility, and successful utilization of solar energy [4]. Whereas, many traditional semiconductors were ultraviolet-light-responsive (ULD) photocatalysts, which could only be excited by ultraviolet light (a small fraction of the solar spectrum, 2%∼4%) [5]. Besides, the rapid recombination of the photo-generated charge carriers in the single-phase photocatalyst also restrict its photocatalytic (PC) activity to a certain extent. Thus, the search of suitable photocatalysts with strong visible light response, high photo-generated carrier separation efficiency and good stability has been an intensively pursued topic [6].

Due to the suitable band gap, easy preparation, good chemical tenability and low-cost, graphitic carbon nitride (g-C_3N_4) has received increasingly attention as one of the most promising metal-free photocatalysts [7]. Although the conduction band (CB) of g-C_3N_4 is sufficiently negative, the PC performance of g-C_3N_4 was far from satisfactory with less positive valance band (VB) and fast recombination of photo-generated electrons and holes. To solve this problem, various attempts have been investigated to improve the visible light photocatalytic efficiency of g-C_3N_4 such as doping with non-metals [8], coupling with metals [9], and combining with semiconductors [10,11]. In particular, semiconductor composite photocatalyst, which construct a heterojunction interface between different components with matching energy levels, could facilitate the interfacial charge transfer and enhance the separation of photo-generated carries [3]. However, the charge

* Corresponding authors at: Key Laboratory of Western China's Environmental Systems (Ministry of Education) and Key Laboratory for Environmental Pollution Prediction and Control, Gansu Province, College of Earth and Environmental Sciences, Lanzhou University, Lanzhou 730000, China.
E-mail addresses: zhangyx@lzu.edu.cn (Y. Zhang), chengxw@lzu.edu.cn (X. Cheng).

https://doi.org/10.1016/j.cclet.2020.04.026

carrier migration in the common p-n heterojunction could reduce both the oxidizing power of holes and the reducing power of electrons, thereby limiting the further exercise of PC activity. Recently, numerous photocatalysts based on Z-scheme heterojunction (*e.g.*, $LaCoO_3$/g-C_3N_4 [12], MoO3/Bi_2O_4 [13], WO_3/MoS_2 [14], *etc.*) have attracted great attention in the field of photocatalysis. It has been accepted that the newly proposed Z-scheme heterojunction could avoid this shortcoming, in which the migration of electrons is from the less negative CB of one semiconductor to the less positive VB of the other semiconductor, thus simultaneously prolonging the lifetime of the more reactive charge carriers and preserving the strong redox ability of remaining electrons and holes [15,16].

In principle, the construction of band match, effective intimate contact interfaces and improved carrier separation efficiency are crucial to efficient Z-scheme photocatalytic system [17]. As an important metal-oxide semiconductor, bismuth(III) oxide (Bi_2O_3) was usually applied as a sensitizer to realize the visible light response [18–20]. By now, six polymorphic forms of Bi_2O_3 have been identified and reported, containing two stable phases (α- and δ-phases) and other four metastable phases (β-, γ-, ε- and ω-phases). Among those polymorphs, α-Bi_2O_3 has been most frequently studied because of its thermal stability and environmental benign characteristics [21]. Notably, benefitting from a less negative CB of Bi_2O_3, which is close to the VB of g-C_3N_4, Bi_2O_3 was considered as a promising candidate for coupling with g-C_3N_4 to construct Z-scheme heterojunction. Moreover, the VB of g-C_3N_4 is about 3.13 eV, positive enough to prompt the photo-generated holes on the VB of Bi_2O_3 to exhibit strong oxidation capacity. So far, there have been some reports on the fabrication of Bi_2O_3/g-C_3N_4 composites for photocatalytic purposes [22]. α-Bi_2O_3 was usually prepared by calcining $Bi(NO_3)_3{\cdot}5H_2O$ crystal, and the morphology of the synthesized α-Bi_2O_3 were mostly granular-shaped or rod-shaped. As far as we know, the related research on the control of the synthesis of α-Bi_2O_3 by introducing precursors has not been reported. Additionally, different preparation methods could obtain Bi_2O_3 samples with different polymorphic forms or different morphology. Consequently, according to previous study, BiOCOOH with Sillen structure has been testified to show satisfying degradation activity under simulated sunlight [23,24]. Despite this, pristine BiOCOOH still suffers from the rapid electron-hole recombination rate, which undermines the photocatalytic performance and restrains the practical application. In this study, we applied BiOCOOH as precursor to obtain α-Bi_2O_3. Besides, since temperature responsible for the morphology, structure and other physicochemical properties of catalysts, and the PC performance of catalysts with different physicochemical characterization vary greatly [25]. Therefore, to explore a new idea of Bi_2O_3 preparation, we optimize the calcination temperature for the photocatalyst synthesis based on BiOCOOH.

Therefore, in this study, α-Bi_2O_3 and g-C_3N_4 were employed to construct a Z-scheme composite photocatalyst through calcination of BiOCOOH/g-C_3N_4 precursors at different temperature. The α-Bi_2O_3/g-C_3N_4 nanocomposite photocatalyst exhibited excellent photocatalytic performance. Subsequently, the effects of various calcination temperatures on the physicochemical properties and photocatalytic efficiencies of as-obtained samples were systematically investigated (Text S1 in Supporting information). Finally, a possible photocatalytic mechanism of the degradation of amido black 10B dye over as-prepared Z-scheme α-Bi_2O_3/g-C_3N_4 composite photocatalyst was proposed.

The information of chemicals which were applied in this study were introduced in Text S2 (Supporting information).

Pure g-C_3N_4 powder was prepared by calcination with dicyandiamide as precursor. Typically, dicyandiamide (3 g) powder was put into an alumina crucible and calcined at 550 °C for 4 h with a rate of 10 °C/min. The resulting yellow product was collected and ground into powders for further use. BiOCOOH/g-C_3N_4 precursor was prepared by a hydrothermal method as follow: 1 mmol $Bi(NO_3)_3{\cdot}5H_2O$ was dissolved in 5 mL DMF by stirring. Subsequently, the solution was added into 40 mL deionized water containing 1 mmol g-C_3N_4 powder and ultrasonication for 10 min to ensure that all of the reagents were dispersed homogeneously. Afterwards, the resulting solution was transferred into the Teflon-lined autoclave, which was maintained at 120 °C for 12 h and then cooled to room temperature naturally. The obtained precipitates were collected and washed for several times with deionized water and absolute ethanol, respectively. Finally, the products were dried at 60 °C. At this point, the precursor BiOCOOH/g-C_3N_4 was obtained. The pure BiOCOOH was synthesized following the above procedures without the addition of g-C_3N_4. For the preparation of the α-Bi_2O_3/g-C_3N_4 composites, the BiOCOOH/g-C_3N_4 precursor was put in a covered crucible and calcined at a certain temperature (T = 300, 400, 450, 500 °C) for 3 h. The final as-obtained samples with different calcination temperature (300, 400, 450, 500 °C) were respectively denoted as BC-300, BC-400, BC-450, and BC-500. The B-400 sample is the one synthesized similarly but without the addition of g-C_3N_4.

In this work, amido black 10B dye was used as representative pollutants to estimate the PC activity of the prepared samples. The PC reaction was carried out at room temperature in 80 mL quartz reactor containing 20 mg as-prepared photocatalysts and 50 mL amido black 10B aqueous solution of 10 mg/L. A 35 W xenon lamp with light density of 67 mW/cm^2 was served as the external light source. Prior to irradiation, the suspensions were magnetically stirred in the dark for about 60 min to ensure the establishment of an adsorption-desorption equilibrium. Subsequently, the xenon

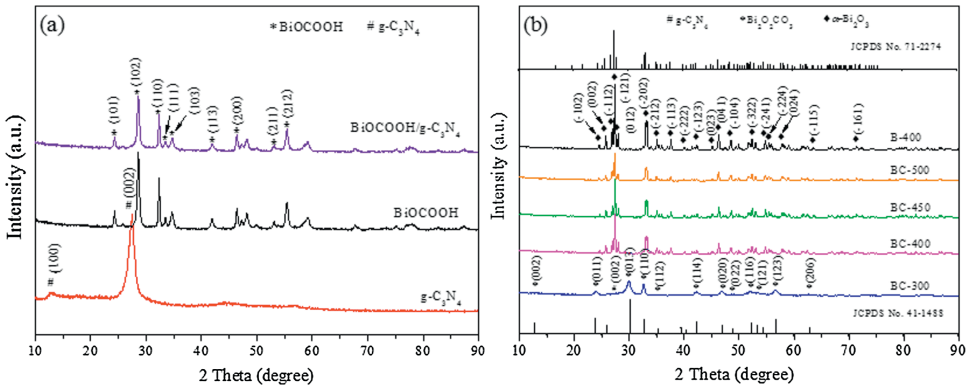

Fig. 1. XRD patterns of as-prepared photocatalysts.

lamp was switched on. At given time intervals, certain amount of the solution after taking from the reactor and filtering through a 0.45 μm membrane filter were measured at the characteristic wavelength of 613 nm using an Evolution 300 UV–vis spectrophotometer.

Fig. 1 displayed the XRD spectra of g-C_3N_4, BiOCOOH, BiOCOOH/g-C_3N_4 and the calcination products of BiOCOOH/g-C_3N_4. Obviously, pure g-C_3N_4 sample (Fig. 1a) showed two typical diffraction peaks at 13.09° and 27.47°, corresponding to the (100) and (002) crystal planes of g-C_3N_4 (JCPDS No. 87-1526), respectively [26]. All the diffraction peaks of the as-prepared BiOCOOH sample could be readily indexed to the tetragonal BiOCOOH (JCPDS No. 35-0939), which was in good agreement with previous reported literatures [27]. Only the characteristic peaks assigned to BiOCOOH were observed in the BiOCOOH/g-C_3N_4 composite, which might be ascribed to the low crystallinity of g-C_3N_4. Similar phenomenon was also observed in g-C_3N_4/Bi_4O_7 [28] and $BiOIO_3$/g-C_3N_4 heterostructured composite [3]. Fig. 1b exhibited the XRD patterns of the samples after the 300–500 °C calcination of the precursor BiOCOOH/g-C_3N_4 composite. Obviously, the sample obtained after 300 °C calcination was $Bi_2O_2CO_3$/g-C_3N_4 composite because the main detectable diffraction peaks of BC-300 could be matched with the tetragonal phase of $Bi_2O_2CO_3$ according to the PDF card (JCPDS NO. 41-1488) [29] and the small peak at 27.4° represented the (002) planes of g-C_3N_4. The generation of $Bi_2O_2CO_3$ was due to the following reaction between BiOCOOH and O_2 at 300 °C (Eq. 1):

$$2BiOCOOH + O_2 \rightarrow Bi_2O_2CO_3 + H_2O + CO_2 \quad (1)$$

However, after calcination at 400 °C, the diffraction peaks of $Bi_2O_2CO_3$ was disappeared and the major characteristic peaks at around 24.58°, 25.75°, 26.90°, 27.40°, 28.01°, 33.25°, 35.03°, 37.63°, 39.94°, 42.11°, 44.92°, 46.37°, 48.60°, 52.20°, 54.78°, 55.43°, 57.72°, 63.58° and 71.40° should be attributed to the (-102), (002), (-112), (-121), (012), (-202), (-212), (-113), (-222), (-123), (023), (041), (-104), (-322), (-241), (-224), (024), (-115) and (-161) lattice planes of monoclinic α-Bi_2O_3 (JCPDS No. 71-2274) [30]. This illustrated that the α-Bi_2O_3/g-C_3N_4 composite was obtained successfully. This phenomenon could be explained by the fact that when the calcination temperature reached to 400 °C or higher, BiOCOOH would be constantly oxidized by fully reaction with the O_2 in the air atmosphere and eventually transformed to Bi_2O_3. The characteristic peak of g-C_3N_4 was not detected in the α-Bi_2O_3/g-C_3N_4 composite sample because of the overlapping between the sharp peaks of (120) crystal plane of α-Bi_2O_3 at 27.41° and (002) crystal plane of g-C_3N_4 at 27.47° [31]. Besides, as for B-400, there was the detection of monoclinic α-Bi_2O_3 without other impurity peaks, proving that α-Bi_2O_3 could be controllably synthesized through the calcination of BiOCOOH. Notably, the XRD peaks intensity of α-Bi_2O_3 decreased and the diffraction peaks appeared to be blunt as the calcination temperature rose from 400 °C to 500 °C, which indicated that the increase of temperature would affect the crystallinity of the α-Bi_2O_3/g-C_3N_4 composite.

Fig. S1 (Supporting information) showed the FT-IR spectra of g-C_3N_4, B-400, BC-300, BC-400, BC-450 and BC-500 composites, in which the surface functional groups and bonding methods of the as-prepared samples were further explored. For g-C_3N_4 sample, the sharp peak in 808 cm^{-1} could be assigned to the typical breathing vibration of the triazine unites [32]. The strong band from 1200 cm^{-1} to 1600 cm^{-1} were corresponding to the typical stretching modes of C—N heterocycles. Typically, the bands at 1241 cm^{-1} and 13,234 cm^{-1} were ascribable to stretching vibration of connected units of C-N(-C)-C (full condensation) or C—NH—C (partial condensation). While those at 1406, 1458, 1571, and 1641 cm^{-1} were due to typical stretching vibration modes of heptazinederived repeating units [33]. In addition, the broad band located at 3000~3500 cm^{-1} were caused by the stretching vibration of the N—H, indicating the g-C_3N_4 obtained was of incomplete polycondensation [34]. For α-Bi_2O_3, it was known that absorption bands at 423 cm^{-1} and 844 cm^{-1} were due to the symmetrical stretching vibration of Bi—O bond of BiO_3 species [35]. Whereas, the peak at 504 cm^{-1} was due to the stretching vibration of Bi—O bonds of BiO_6 octahedral [36]. Furthermore, the peak at 1390 cm^{-1} was attributed to Bi—O stretching vibration [33]. It was clear that the FT-IR spectrum of B-400 shows the characteristic bands of α-Bi_2O_3, suggesting the generation of α-Bi_2O_3, in consistent with XRD. As for the BC-400, BC-450, and BC-500 samples, the typical bands of α-Bi_2O_3 and g-C_3N_4 could be observed, which could be fully demonstrated that α-Bi_2O_3/g-C_3N_4 can be obtained by calcination of BiOCOOH/g-C_3N_4 precursors. It was worth mentioning that with the increase of temperature, the spectra display clear vibration modes of α-Bi_2O_3. However, the band vibration of g-C_3N_4 could not be obviously observed. This may be due to the fact that high temperature might break the vibration mode of g-C_3N_4 as well as its response of FT-IR.

The morphology and microstructure of as-prepared samples were investigated by SEM and TEM measurement. Fig. 2 showed the SEM images of the pure g-C_3N_4, BiOCOOH/g-C_3N_4 precursors and

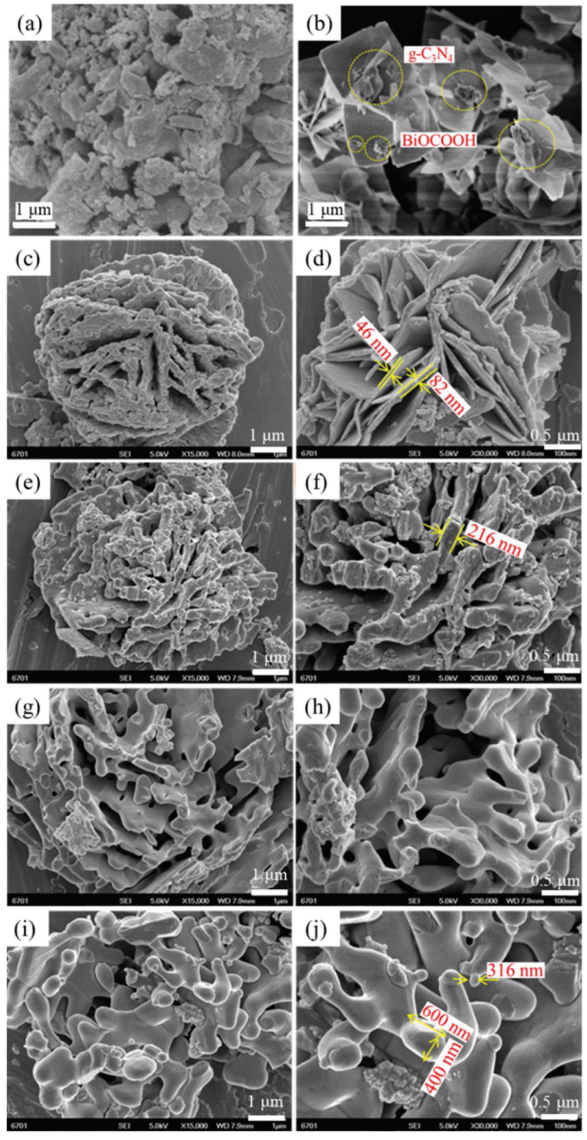

Fig. 2. SEM images of g-C_3N_4 (a), BiOCOOH/g-C_3N_4 (b), BC-300 (c, d), BC-400 (e, f), BC-450 (g, h) and BC-500 (i, j) composites.

α-Bi_2O_3/g-C_3N_4 composites obtained at different calcination temperature. The pure g-C_3N_4 (Fig. 2a) displayed a typically aggregated morphology with a number of micrometer size block-based flakiness and particles. Without calcination, the BiOCOOH/g-C_3N_4 precursor (Fig. 2b) exhibited a flower-like microsphere. The close-packed microflowers consisted of two-dimensional thin flakes with thickness of 30∼50 nm and edge lengths of 1∼2 μm. Besides, many agglomerates of g-C_3N_4 with a diameter of 0.5∼1 μm irregularly attached on the surface of thin flakes. After 300 °C calcination (Figs. 2c and d), the surface of the precursor layer became matte, which might be attributed to the fact that a large amount of small molecular gas, such as CO_2 and H_2O, were released from the precursor during calcination. Consequently, the numerous small pores appeared on the surface of the flower-like microspheres. At this point, the thickness of petals layer were in range of 46∼82 nm. Seen from the Figs. 2e–j, when the calcination temperatures were between 400∼500 °C, the flower-like microsphere morphology of precursors were basically maintained in the as-obtained samples. However, the thickness of the lamella that made up the microflowers increased obviously, while the spherical particles gradually formed and adhered to its surface. This phenomenon could be explained as the increase of calcination temperature leads to the collapse of laminar structure. Notably, as the calcination temperature increases, the diameter of the spherical particles became larger and the surface became smoother. Interestingly, the rod-like structure with a diameter of 400 nm and length of 600 nm even appeared in the samples after calcination at 500 °C.

Fig. S2a (Supporting information) exhibited the TEM images of as-obtained BC-400 composite which showed a stack-morphology. The large black area represented the α-Bi_2O_3, while a few bits of grey agglomerates with irregular morphology were belonged to g-C_3N_4. The corresponding HR-TEM image (Fig. S2b in Supporting information) further displayed the existence of the heterojunction between g-C_3N_4 and α-Bi_2O_3, and the lattice fringes of 0.324 nm could be well agreed with the spacing of (120) planes of α-Bi_2O_3 [37]. It is obvious that there was the formation of heterojunction between g-C_3N_4 and α-Bi_2O_3 in BC-400 composite.

To further examine the surface chemical state and composition of α-Bi_2O_3/g-C_3N_4 composite, XPS analysis was employed. Fig. S3a (Supporting information) displayed the full-scan XPS spectra of BC-400 sample, wherein C, N, O, Bi species were detected. As illustrated in Fig. S3b (Supporting information), two peaks at 284.8 and 288.1 eV could be observed in the high-resolution spectrum of C 1s. The characteristic peaks could be assigned to carbon atoms (C—C bonding) in a carbon environment; *i.e.*, amorphous carbon adsorbed on the surface and carbon atoms bond in N-containing aromatic rings (N—C=N) in the pure g-C_3N_4 and BC-400 composite [37]. The high-resolution spectrum of N 1s (Fig. S3c in Supporting information) could be described as the superposition of three peaks located at 398.5, 399.9 and 401.1 eV. The binding energies at 398.5 and 401.1 eV were corresponded to sp^2-bonded N in the triazine rings (C—N=C) and amino groups (C—N—H), respectively. While the peak at 399.9 eV belongs to the tertiary N in the form of N-$(C)_3$ group. Apart from these, there was a weakest peak at 404.3 eV (π-excitations) could be detected in pure g-C_3N_4, but the binding energies shifted to 404.8 eV in the BC-400 composite. It implied that α-Bi_2O_3 affected the π-excitations and coupled with g-C_3N_4 *via* an interaction using π-electrons of CN heterocycles, rather than combined with sole C or N atoms of g-C_3N_4 [38]. As for the Bi 4f XPS spectrum (Fig. S3d in Supporting information), two binding energies at 158.7 and 164.1 eV of BiOCOOH/g-C_3N_4 were attributed to Bi $4f_{7/2}$ and Bi $4f_{5/2}$, respectively. It demonstrated that Bi species existed in the forms of Bi^{3+} in composite [27]. Notably, the binding energies of Bi in BC-400 exhibited a negative shift relative to those of BiOCOOH/g-C_3N_4, which could be attributed to the generation of α-Bi_2O_3 as well as the interaction of g-C_3N_4 with α-Bi_2O_3, resulting in inner shift of Bi 4f orbits. And the peaks at 158.5 and 163.8 eV were respectively corresponded to the Bi $4f_{7/2}$ and Bi $4f_{5/2}$ of α-Bi_2O_3. Similarly, the peaks of O 1s (Fig. S3e in Supporting information) were also changed, and the binding energy at 529.5 eV could be indexed to the lattice oxygen of Bi—O bonds in $[Bi_2O_2]^{2+}$ slabs in BiOCOOH, while peak at 529.2 eV was characteristic of Bi—O binding energy in Bi_2O_3. The slight in lower binding energy could be attributed to the increased electron density in α-Bi_2O_3/g-C_3N_4 [39]. Besides, another two peaks with the binding energy of 531.2 and 532.9 eV were attributed to the hydroxyl groups or carboxyl groups [40]. In summary, the XPS results indicated that both g-C_3N_4 and α-Bi_2O_3 existed in the BC-400 composite. And all the observed shifts for binging energy were ascribed to the intense interaction between α-Bi_2O_3 and g-C_3N_4, further confirming the establishment of the heterojunctions.

In order to explore the porous properties of as-prepared samples, the BET surface area and pore size distribution were measured *via* N_2 adsorption-desorption isotherms method. According to the IUPAC classification, the N_2 adsorption-desorption isotherms curve of all samples could be classified as type IV isotherms as shown in Fig. S4 (Supporting information), indicating that the sample have mesoporous structure [22]. Besides, the adsorption isotherms were below the desorption isotherm corresponding to the type H_3 hysteresis loop, and this adsorption hysteresis was usually attributed to the size and shape of pores [41]. The corresponding pore size distributions of samples were shown in the inset of Fig. S4, which further indicated the presence of mesoporous, and pore size of mesoporous were not uniform ranging from 5 nm to 60 nm. The BET surface area, pore volume and pore diameter of as-prepared samples were displayed in the Table S1 (Supporting information). It can be seen that the BET specific surface area of α-Bi_2O_3/g-C_3N_4 calcined by 400, 450 and 500 °C were 8.149, 7.214, and 4.632 mg^2/g, respectively, which were significantly smaller than that of BiOCOOH/g-C_3N_4. And the specific surface area of resulting α-Bi_2O_3/g-C_3N_4 composite gradually decreased with the increase of temperature.

The optical properties of as-prepared catalysts, which were important indicator for evaluating PC performance [42], were studied and illustrated *via* UV–vis DRS. As illustrate in Fig. S5a (Supporting information), it was observed that the steep absorption edge of B-400 was about 447 nm, and the pure g-C_3N_4 exhibited absorption wavelengths from the UV to the visible range up to 464 nm. However, compared with pure g-C_3N_4, the absorption wavelength regions of the BC-X composites showed slight blue shift, except for BC-300 sample. It might be attributed to the interaction between the g-C_3N_4 and α-Bi_2O_3 and smaller specific surface area of α-Bi_2O_3/g-C_3N_4 composite.

As is well-known that for a crystalline semiconductor, the band gap energy (E_g) could be calculated by the following Kubelka-Munk transformation (Eq. 2) [22]:

$$\alpha h\nu = A(h\nu - E_g)^{2/n} \quad (2)$$

where α, h, ν, A, and E_g are absorption coefficient, Planck constant, light frequency, proportionality and band gap energy, respectively. n is corresponding to the properties of the transition in a semiconductor (n = 1 for direct transition and n = 4 for indirect transition). For g-C_3N_4 and Bi_2O_3, the values of n are 4 and 1, respectively. By applying this equation, the band gap of g-C_3N_4 and B-400 is 2.71 and 3.48 eV, respectively, which agrees with the previous reports [37]. The result was illustrated in Fig. S5b (Supporting information). Furthermore, the band position of

photocatalyst could be also calculated by the following empirical formulas (Eqs. 3 and 4) [43]:

$$E_{VB} = X + 0.5E_g - E^e \quad (3)$$

$$E_{CB} = E_{VB} - E_g \quad (4)$$

where E_{VB} is the valence band potential; E_{CB} is the conduction band potential; X is the absolute electronegativity of the semiconductor; E^e is the energy of free electrons on the hydrogen scale (E^e = 4.5 eV). The X values for g-C_3N_4 and Bi_2O_3 are 4.73 and 6.23 eV, respectively [22,44]. By calculation, the E_{VB} and E_{CB} of g-C_3N_4 were about 1.58 and -1.13 eV, respectively, while the E_{VB} and E_{CB} of g-C_3N_4 were about 3.13 and 0.33 eV, respectively.

Photoelectrochemical measurements were employed to further qualitatively confirm the enhanced migration and separation of photo-generated charge carries in this study. Fig. 3a performed the transient photocurrent-curves of g-C_3N_4, B-400 and BC composites obtained by calcination at different temperature with typical on-off cycles under 35 W xenon lamp irradiation. Generally, the higher photocurrent intensity means higher separation efficiency of photo-generated charge carriers, which might cause superior PC activity. Obviously, the photocurrents of all composite samples were significantly higher than that of pure samples, which indicated that the heterojunction structure formed by combination of α-Bi_2O_3 and g-C_3N_4 was conducive to the effective separation of electron-hole pairs. It is noteworthy that the BC-400 sample was the most prominent one among them. It performed an enhanced transient photocurrent response with a photocurrent density of 1.0 μA/m^2, which was nearly 6.67 folds higher than that of pure α-Bi_2O_3 and g-C_3N_4 (0.15 μA/m^2) under same condition. This revealed that a smaller recombination and a more efficient separation of photo-generated charge carries occurred at the interface between α-Bi_2O_3 and g-C_3N_4 in BC-400 nanocomposite. Moreover, all photocatalysts showed good repeatability and stability under several on-off cycles of intermittent illumination, indicating that the electrodes were stable and the responses were reversible. Besides, EIS measurement conducted at the open circuit potential with 35 W xenon lamp illumination was carried out to clarity the electrical conductivity of all samples. As shown in Fig. 3b, BC-400 sample exhibited the smallest arc radius on the EIS plots, indicating that the minimum charge transfer resistance existed in the BC-400 composite, which was conducive to the separation and migration of photo-generated charge carriers [45]. This phenomenon was well identical to the results of transient photocurrent measurement. Moreover, Mott-Schottky (M-S) plots of the g-C_3N_4 and BC-400 composite were carried out in the dark with a frequency of 1000 Hz. As demonstrated in Fig. 3c, the positive slopes of the plots revealed that g-C_3N_4 and BC-400 composite were n-type semiconductor. And the plots were extrapolated to $1/C^2 = 0$ to estimate the values of flat band potential (E_{FB}), giving -0.32 and -0.57 V for g-C_3N_4 and BC-400 composite, respectively. The negative shift of E_{FB} in BC-400 composites demonstrated an increase in bending of the band edge after combining α-Bi_2O_3 with g-C_3N_4, which was benefit for the separation and transportation of photo-generated charge carriers. Based on the above discussion, the enhanced PC performance of α-Bi_2O_3/g-C_3N_4, especially BC-400 composite, could be anticipated.

In this work, amido black 10B dye was served as representative organic pollutants to evaluate the PC activities of a series of BC composites obtained at different calcination temperature. Meanwhile, the PC performances of pure g-C_3N_4 were also measured as references. As depicted in Fig. 4a, the degradation of amido black 10B could be almost neglected in the absence of photocatalysts after 120 min of reaction through blank test, which indicated that amido black 10B was a stable dye molecule with weak self-photolysis. The PC degradation of pure g-C_3N_4 for amido black 10B was 62.89%, which was lower than that of composite photocatalysts. However, the degradation rate was significantly enhanced when α-Bi_2O_3 was used to combine with g-C_3N_4 to prepared nanocomposite photocatalyst. And the PC efficiency of α-Bi_2O_3/g-C_3N_4 composts with different calcination temperature (400∼500 °C) were 97.09%, 95.97%, and 85.62%, respectively. Apparently, α-Bi_2O_3/g-C_3N_4 photocatalyst that was calcined at 400 °C exhibited the highest PC efficiency, which mainly ascribed to the intense visible light absorbance and high separation efficiency of electron and hole pairs. However, the PC activity decreased as further increase of calcination temperature. Combined with the analysis of SEM, this phenomenon could be interpreted that the calcination temperature has a dramatically impact on the morphology of catalysts. In detail, the higher calcination temperature was, the more obvious the agglomeration would be formed. More importantly, excessive agglomeration of nanocomposite would be unfavorable to the charge transfer, thereby weakening the PC efficiency [46]. This was accordance with the above results of the PECH characterization.

Furthermore, kinetics of PC degradation of amido black 10B dye under 35 W xenon lamp light irradiation over all as-fabricated catalysts were investigated by applying the Langmuir-Hinshelwood (L-H) model with 120 min. After fitting, the plots -ln(C/C_0) *versus* irradiation time t were found to be linear as displayed in Fig. 4b, implying that the photodecomposition reactions followed the pseudo-first order kinetics. The apparent reaction rate constants (k) of pure g-C_3N_4, BC-300, BC-400, BC-450, and BC-500 samples were determined to be 0.00751, 0.01958, 0.02661, 0.02501, and 0.01578 min^{-1}, respectively. Obviously, compared with other four samples, BC-400 present the best photocatalytic performance and held the highest rate constant.

Distinguishing the construction of each primary reactive species to the PC activity was critical to the analytical of PC mechanism. Thus, reactive species trapping experiments was

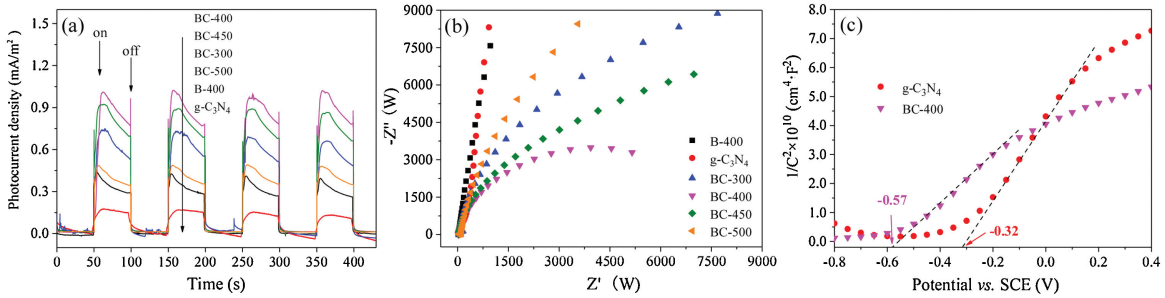

Fig. 3. (a) Transient photocurrent-curves and (b) EIS curves of g-C_3N_4, B-400 and BC composites obtained at different calcination temperatures; (c) Mott-Schottky plots of g-C_3N_4 and BC-400 composite.

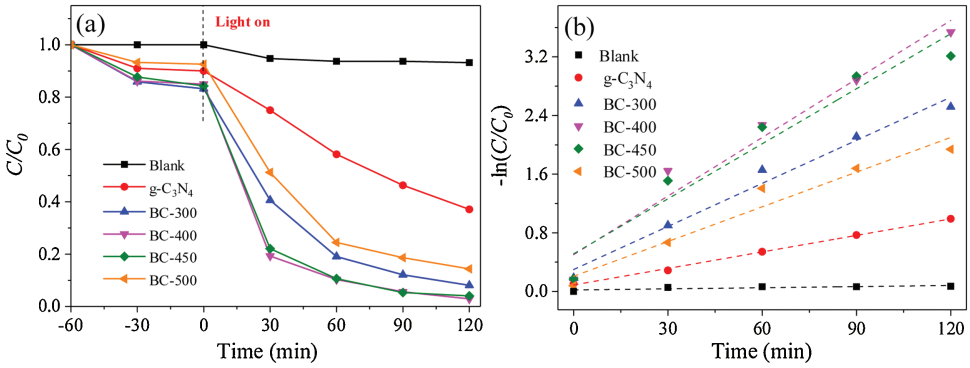

Fig. 4. Successive photocatalytic degradation rate (a) and the first-order kinetics (b) of amido black 10B by g-C_3N_4 and BC composites obtained at different calcination temperature.

carried out during the PC degradation processes, in which ammonium oxalate (AO), isopropanol (IPA) and benzoquinone (BQ) were selected as the quenchers of h^+, $^{\bullet}OH$ and $O_2^{\bullet-}$, respectively [46]. Fig. S6 (Supporting information) showed the effects of different scavengers on the photocatalytic degradation of amido black 10B over BC-400 photocatalyst after 120 min illumination. It could be obviously found that the addition of IPA has a little effect on the PC performance of BC-400, which indicated that $^{\bullet}OH$ played a minor role in the photocatalytic reaction. On the contrary, the PC degradation efficiency was significantly decreased when the AO and BQ were added, demonstrating both h^+ and $O_2^{\bullet-}$ were the main active species in the degradation of amido black 10B under visible-light irradiation.

As suggested above, a possible photocatalytic degradation mechanism of amido black 10B by the α-Bi_2O_3/g-C_3N_4 composite photocatalyst under visible light irradiation was illustrated in Fig. S7 (Supporting information). When α-Bi_2O_3 and g-C_3N_4 were combined with each other, interfacial heterojunction structure would be formed because of their firm contacting. And owing to the narrow band gap and good light absorption abilities of α-Bi_2O_3 and g-C_3N_4, both of them could be easily excited to generate photo-induced electron-hole pairs under visible light illumination. Since the E_{CB} of g-C_3N_4 (-1.12 eV *vs.* NHE) was more negative than the standard redox potential of $O_2/O_2^{\bullet-}$ (-0.33 eV *vs.* NHE) [31], the electros in the CB of g-C_3N_4 would be available to reduce the surface chemisorbed O_2 to produce $O_2^{\bullet-}$, which could decompose the amido black 10B into other produces and some small molecules. However, the holes in the VB of g-C_3N_4 could not bond with water to oxide OH to give $^{\bullet}OH$ due to the lower VB potential of g-C_3N_4 (1.58 eV *vs.* NHE) than the standard redox potential of $^{\bullet}OH/OH^-$ (2.4 eV *vs.* NHE). This explicated why $^{\bullet}OH$ was not the main reactive species in the photocatalytic process. Similarly, the electrons in the CB of α-Bi_2O_3 also could not reduce O_2 to give $O_2^{\bullet-}$ because of its more positive CB potential than that of E^0 ($O_2/O_2^{\bullet-}$). Therefore, combined with the results of reactive species trapping experiments, the transfer and recombination of photo-generated electros and holes in α-Bi_2O_3/g-C_3N_4 followed the Z-scheme modes, rather than the most common composite photocatalysts [47]. Consequently, when the α-Bi_2O_3/g-C_3N_4 composite was illuminated, photo-generated electrons in the CB of α-Bi_2O_3 would rapidly migrate and recombine with holes in the VB of g-C_3N_4 to form a direct Z-scheme charge separation path. Subsequently, the holes accumulated on the VB of α-Bi_2O_3 would be consumed to directly oxidize amido black 10B. In such a way, the photo-generated charge carries between the α-Bi_2O_3 and g-C_3N_4 could be effectively separated and involved in photocatalytic reactions, thereby resulting in an enhanced visible light PC performance of α-Bi_2O_3/g-C_3N_4 composite. Furthermore, all the processes of photodegradation of amido black 10B over α-Bi_2O_3/g-C_3N_4 composite could be described as follows (Eqs. 5–8):

$$\alpha\text{-}Bi_2O_3/g\text{-}C_3N_4 + h\nu \rightarrow \alpha\text{-}Bi_2O_3\ (e^- \ldots h^+)/g\text{-}C_3N_4\ (e^- \ldots h^+) \quad (5)$$

$$\alpha\text{-}Bi_2O_3\ (e^- \ldots h^+)/g\text{-}C_3N_4\ (e^- \ldots h^+) + h\nu \rightarrow \alpha\text{-}Bi_2O_3\ (h^+)/g\text{-}C_3N_4\ (e^-) \quad (6)$$

$$g\text{-}C_3N_4\ (e^-) + O_2 \rightarrow O_2^{\bullet-} \quad (7)$$

$$\alpha\text{-}Bi_2O_3\ (h^+) + O_2^{\bullet-} + \text{amido black 10B} \rightarrow \text{Other products} + CO_2 + H_2O \quad (8)$$

The stability and reusability were important parameter for photocatalysts in the application of wastewater treatment. Thus, in order to ascertain the stability and practicability of as-prepared α-Bi_2O_3/g-C_3N_4, BC-400 sample which exhibited the best photocatalytic activity was chosen for stability test. As shown in Fig. S8a (Supporting information), the BC-400 composite still remained high photocatalytic efficiency for amido black 10B degradation even after consecutive utilization for four recycles, suggesting that it has prominent photochemical stability. Besides, the XRD pattern of used BC-400 composite (Fig. S8b in Supporting information) also demonstrating a very stable crystal structure of it because of no extra diffraction peaks were observed after four times reuse. At this point, we can reasonably conclude that α-Bi_2O_3/g-C_3N_4 composite has superior stability, which could be used as the promising candidate in wastewater treatment.

In summary, we combined α-Bi_2O_3 with g-C_3N_4 and synthesized direct Z-scheme α-Bi_2O_3/g-C_3N_4 composite photocatalyst through facile calcination of BiOCOOH/g-C_3N_4 at different thermal treatment temperatures. The results of various characterization indicated that synthesized temperature has effects not only on the morphologies and structure of α-Bi_2O_3/g-C_3N_4 composite, but also on its optical and photoelectrochemical properties. With comparison of g-C_3N_4, the prepared α-Bi_2O_3/g-C_3N_4 composite photocatalyst exhibited much higher photocatalytic activity. Particularly, BC-400 composite displayed the highest transient photocurrent response with a photocurrent density of 1.0 $\mu A/m^2$ as well as the best PC efficiency towards the degradation of amido black 10B, which was approximately 1.54 folds than that of pure g-C_3N_4, respectively. Besides, the reactive radical species trapping experiment confirmed that both h^+ and $O_2^{\bullet-}$ were the main active species in the photocatalytic process, while $^{\bullet}OH$ played a relatively small role. The improved PC activity of α-Bi_2O_3/g-C_3N_4 composite could be mainly attributed to the construction of Z-scheme

heterojunction between α-Bi_2O_3 and g-C_3N_4, giving rise to efficient separation of the photog-generated charge carriers and strong redox ability for photocatalytic degradation of organic dye solution. In addition, the good stability and reusability of as-prepared α-Bi_2O_3/g-C_3N_4 composite photocatalyst further indicated that it could be used as the promising candidate for application in wastewater treatment.

Declaration of competing interest

We have no conflicts of interest to declare.

Acknowledgments

This work was kindly supported by the National Natural Science Foundation of China (Nos. 51508254, 51978319), Fundamental Research Funds for the Central Universities (No. lzujbky-2017-it98), College Students' Innovative Practice Training Program of Chinese Academy of Sciences (No. Y710171040) and Key Laboratory of Comprehensive and Highly Efficient Utilization of Salt Lake Resources, Qinghai Institute of Salt Lakes, Chinese Academy of Sciences.

Appendix A. Supplementary data

Supplementary material related to this article can be found, in the online version, at doi:https://doi.org/10.1016/j.cclet.2020.04.026.

References

[1] S.W. Lee, G.V. Lowry, H. Hsu-Kim, Environ. Sci. Process. Impacts 18 (2016) 176–189.
[2] J. Huang, H. Song, C. Chen, et al., J. Environ. Chem. Eng. 5 (2017) 2579–2585.
[3] Y. Gong, X. Quan, H. Yu, et al., Appl. Catal. B: Environ. 237 (2018) 947–956.
[4] X. Cheng, H. Liu, Q. Chen, et al., Electrochim. Acta 103 (2013) 134–142.
[5] L. Tian, L. Xing, X. Shen, et al., Atmos. Pollut. Res. 11 (2020) 179–185.
[6] D. Xia, W. Wang, R. Yin, et al., Appl. Catal. B: Environ. 214 (2017) 23–33.
[7] F. Yu, L. Wang, Q. Xing, et al., Chin. Chem. Lett. 31 (2020) 1648–1653.
[8] Y. Zhou, L. Zhang, W. Huang, et al., Carbon 99 (2016) 111–117.
[9] Y. Yu, S. Cheng, L. Wang, et al., Sustain. Mater. Technol. 17 (2018) e00072.
[10] W. Yu, J. Chen, T. Shang, et al., Appl. Catal. B: Environ. 219 (2017) 693–704.
[11] R. Guo, X. Zhang, B. Li, et al., J. Phys. D-Appl. Phys. 52 (2019)085302.
[12] Z. Jin, R. Hu, H. Wang, et al., Appl. Surface Sci. 491 (2019) 432–442.
[13] T. Jiang, K. Wang, T. Guo, et al., Chin. J. Catal. 41 (2020) 161–169.
[14] G. Li, J. Hou, W. Zhang, et al., Mater. Chem. Phys. 246 (2020)122827.
[15] L. Cui, D. Xiang, Y. Wang, et al., Appl. Surface Sci. 391 (2016) 202–210.
[16] Y. Hong, C. Li, B. Yin, et al., Chem. Eng. J. 338 (2018) 137–146.
[17] Z.-F. Huang, J. Song, X. Wang, et al., Nano Energy 40 (2017) 308–316.
[18] G. Liu, S. Li, Y. Lu, et al., J. Alloys. Compd. 689 (2016) 787–799.
[19] T.A. Gadhi, A. Hernandez-Gordillo, M. Bizarro, et al., Ceram. Int. 42 (2016) 13065–13073.
[20] Z. Liang, Y. Cao, Y. Li, et al., Appl. Surface Sci. 390 (2016) 78–85.
[21] Y. Qiu, J. Zhou, J. Cai, et al., Chem. Eng. J. 306 (2016) 667–675.
[22] J. Zhang, Y. Hu, X. Jiang, et al., J. Hazard. Mater. 280 (2014) 713–722.
[23] S. Li, J. Chen, Y. Liu, et al., J. Alloys. Compd. 781 (2019) 582–588.
[24] J. Xu, Y. Wang, J. Niu, et al., Sep. Purif. Technol. 225 (2019) 24–32.
[25] X. Cui, Y.F. Zheng, H. Zhou, et al., J. Taiwan Instit. Chem. Eng. 60 (2016) 328–334.
[26] L. Ge, C. Han, Appl. Catal. B: Environ. 117-118 (2012) 268–274.
[27] P. Chen, Q. Zhang, Y. Su, et al., Chem. Eng. J. 332 (2018) 737–748.
[28] M. Sun, Y. Wang, Y. Shao, et al., J. Colloid Interface Sci. 501 (2017) 123–132.
[29] W. Shan, Y. Hu, Z. Bai, et al., Appl. Catal. B: Environ. 188 (2016) 1–12.
[30] S. Sood, A. Umar, S. Kumar Mehta, et al., Ceram. Int. 41 (2015) 3355–3364.
[31] Y. Cui, X. Zhang, R. Guo, et al., Sep. Purif. Technol. 203 (2018) 301–309.
[32] M.J. Bojdys, J.-O. Müller, M. Antonietti, et al., Chem. Eur. J. 14 (2008) 8177–8182.
[33] M. Xiong, L. Chen, Q. Yuan, et al., Carbon 86 (2015) 217–224.
[34] Y. Bu, Z. Chen, J. Yu, et al., Electrochim. Acta 88 (2013) 294–300.
[35] K.K. Bera, R. Majumdar, M. Chakraborty, et al., J. Hazard. Mater. 352 (2018) 182–191.
[36] Y. Li, S. Wu, L. Huang, et al., J. Phys. Chem. Sol. 76 (2015) 112–119.
[37] D. Chen, S. Wu, J. Fang, et al., Sep. Purif. Technol. 193 (2018) 232–241.
[38] A. Thomas, A. Fischer, F. Goettmann, et al., J. Mater. Chem. 18 (2008) 4893–4908.
[39] J. Lu, J. Sun, X. Chen, et al., Chem. Eng. J. 358 (2019) 48–57.
[40] B. Chai, X. Wang, RSC Adv. 5 (2015) 7589–7596.
[41] X. Gao, R. Zhang, Y. Shang, et al., J. Phys. Chem. Sol. 119 (2018) 19–28.
[42] S. Chen, Y. Hu, S. Meng, et al., Appl. Catal. B: Environ. 150–151 (2014) 564–573.
[43] Y. Cui, L. Nengzi, J. Gou, et al., Sep. Purif. Technol. 232 (2020) 115959.
[44] B. Lin, H. Li, H. An, et al., Appl. Catal. B: Environ. (2017) 542–552.
[45] K. Kadeer, Y. Tursun, T. Dilinuer, et al., Ceram. Int. 44 (2018) 13797–13805.
[46] Y. Cui, Q. Ma, X. Deng, et al., Appl. Catal. B: Environ. 206 (2017) 136–145.
[47] L. Yang, P. Wang, J. Yin, et al., Appl. Catal. B: Environ. 250 (2019) 42–51.